High-Resolution Imaging Capability of Large-Scale LEO Satellite Constellations

Lhamo Dorje, Xiaohua Li, Yu Chen, Nihal A Poredi

Department of Electrical and Computer Engineering, Binghamton University, Binghamton, NY 13902, USA

{ldorje1, xli, ychen, nporedi1}@binghamton.edu

Abstract—There has been a great interest in deploying large-scale Low-Earth Orbit (LEO) satellite constellations for wireless communications. This paper shows that LEO satellite constellations developed for communication purposes can be exploited for ground target imaging applications, where a unique advantage is to achieve super-high imaging resolutions that are not achievable via other imaging techniques. A new imaging algorithm is developed for this novel integrated sensing and communication (ISAC) application based on delay-sensitive signal processing and irregular sensing data exploitation. Imaging performance is analyzed. Simulations with the practical SpaceX Starlink satellite orbital data are conducted to verify both the new algorithm and the analysis results. This paper demonstrates that while the resolution of conventional satellite imaging is limited to sub-meters, the new method can potentially use only a small set of LEO satellites to achieve sub-centimeter resolution.

Index Terms—Millimeter-wave imaging, LEO satellite constellation, Synthetic aperture radar (SAR), Integrated Sensing and Communication (ISAC), Starlink

I. INTRODUCTION

It is expected that the future sixth-generation (6G) mobile communications will see the convergence of terrestrial and satellite communications [1], where one of the major directions is to deploy large-scale Low-Earth Orbit (LEO) satellite constellations to support global mobile broadband communications, even over the seas or in remote areas that do not have traditional mobile communication support [2]. Several LEO satellite constellations have already been in use [3]: The Telesat system comprises 117 satellites; the OneWeb system comprises 720 satellites; and the well-known SpaceX Starlink system has over 3000 satellites deployed in space already, with over 50,000 satellites in planning. Especially, the success of the SpaceX Starlink system has stimulated many other companies and countries to develop their own large-scale LEO satellite constellations.

These constellations are mainly designed for communications because only the large mobile communications market can defray the huge deployment and maintenance costs. Nevertheless, it is highly desirable to reuse them as sensing platforms to add extra sensing values, which has been largely an open problem [4].

Space-borne sensing has a lot of unique applications. One of the important applications is to generate ground images, either optical images or synthetic aperture radar (SAR) images. Commercially available satellite imaging has a resolution limited

to around 0.25 meters, for both optical and SAR imaging. As the state-of-the-art, some classified satellite imaging systems may have an augmented resolution of up to 0.1 meters. It has been difficult to further increase the resolution for better recognizing finer targets [5].

This paper shows that large-scale LEO satellite constellations have the unique capability of imaging ground targets at a super-high resolution of sub-centimeters, an order of magnitude higher than today's state-of-the-art. Such a high resolution is almost impossible to achieve with traditional satellite imaging techniques that are limited to using a single satellite. As a novel integrated sensing and communication (ISAC) application, the new imaging method reuses communications satellites for sensing purposes without any hardware change, nor requiring any extra radar transceivers.

The new imaging method relies on many satellites to work jointly to generate an image. The imaging principle is similar to that of the millimeter-wave/Tera-Hz (THz) imaging used in, e.g., airport screening systems [6][7][8]. Nevertheless, there are many important differences to deal with, such as larger delay, faster movement, larger Doppler shift, and weaker signal strength. The most fundamental difference is that traditional millimeter-wave or THz imaging uses large 2D or 3D antenna arrays with antennas evenly spaced at a half-wavelength regular distance. For example, an array using 736 transmit (Tx) antennas and 736 receive (Rx) antennas to electronically scan 25,600 antenna positions within a regular grid of 50cm×50cm aperture was proposed in [8]. This kind of scan over a 2D regular grid is impossible for satellites. In contrast, our new method does not require a regular sensor grid. It exploits the data acquired by satellites at any arbitrary locations along their flight trajectories.

The organization of this paper is as follows. Section II describes the satellite constellation imaging model. Section III develops the imaging algorithm and studies its performance. Section IV presents simulation and experiment results. Conclusions are given in Section V.

II. SYSTEM MODEL

Large-scale LEO satellite constellations such as the Starlink create a cellular structure similar to mobile networks, with satellite antenna beams replacing terrestrial cellular towers [9]. At any given time, a cell on the ground is illuminated by one or more beams. The size of the cell is determined by the beam width. Each satellite beam only serves this cell for a short time.
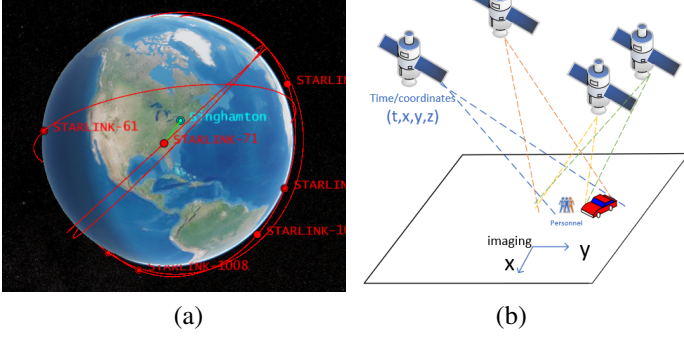
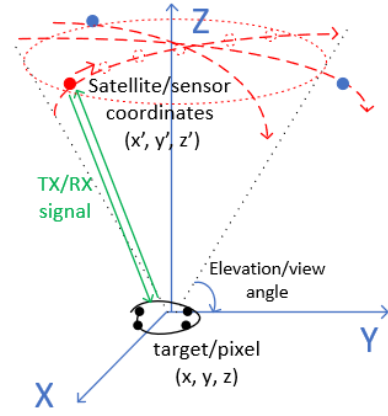Fig. 1. (a) Satellite orbits. (b) Satellites jointly image a ground target.

Fig. 2. Coordinates of the satellites and targets. A valid satellite (red dot) enters the sensing area (red dotted circle) and collects sensing data at various locations along its orbit trajectory.

The cell is continuously served by the satellites flying over, as shown in Fig. 1 (a).

Conventional satellite SAR imaging [10][11] uses a single satellite only to generate an image. The range (Y-direction in Fig. 1) resolution is $\Delta Y = \frac{c}{2B}$, where c is the speed of light and B is the signal bandwidth. For example, Starlink has a beam signal bandwidth of 250 MHz, so the SAR imaging resolution is 0.6 meters. The resolution is fundamentally limited by B or the available spectrum resource. It is not likely to assign tens of GHz bandwidth to satellite imaging applications in the RF or microwave band. The millimeter-wave or THz bands are not suitable for long-distance satellite transmissions due to the heavy propagation loss. Therefore, it is hard, if not impossible, to achieve sub-centimeter or millimeter-level resolution with conventional techniques.

By contrast, LEO satellite constellations provide a new way to enhance the imaging resolution by orders of magnitude. Fig. 1 (b) illustrates the new concept of using multiple satellites to jointly image ground targets. When a satellite flies over a target area, it illuminates the target and records the reflected echoes. Multiple satellites within this area can transmit and receive at the same time with orthogonal beam signals. These satellites are called *valid* satellites and their data are collected and processed together to generate an image of the target. These valid satellites effectively form a virtual antenna array. The size of the array is the synthetic aperture which determines the imaging resolution.

Consider the imaging configuration in Fig. 2, a satellite moves along a trajectory $\mathbf{r}' = (x', y', z')$ while imaging a target located at $\mathbf{r} = (x, y, z)$. It transmits signal $p(t)$ and receives the echo signal

$$\hat{s}_{\mathbf{r}'}(t) = \int_{\mathbf{r}} \sigma_{\mathbf{r}} p(t - \tau_{\mathbf{r}'\mathbf{r}}) d\mathbf{r} + \hat{v}_{\mathbf{r}'}(t), \qquad (1)$$

where $\tau_{\mathbf{r}'\mathbf{r}}$ is the propagation delay, $\sigma_{\mathbf{r}}$ is the target reflection coefficient, and $\hat{v}_{\mathbf{r}'}(t)$ includes any unwanted noise, interference, and clutter [12]. The signal is processed to generate an image based on the SAR principle.

The satellites can transmit either radar signals such as Frequency-Modulated Continuous Wave (FMCW) [10] or communication signals such as Digital Video Broadcasting - Satellite - 2nd Generation (DVB-S2X) signal waveform [13],

the fifth generation (5G) mobile signal waveform, etc. Reusing communication signals directly for sensing is more attractive because it reduces hardware complexity and cost. Especially, while one satellite is transmitting signals to ground receivers for communications purposes, the receivers on this satellite and other valid satellites can passively receive the echoes simultaneously for sensing and imaging purposes. There is no need to switch between the communication mode and the sensing mode. There is no need for extra circuits of radar signal modulation/demodulation.

However, reusing satellite communication signals for SAR imaging is a completely new problem. Conventional satellite SAR imaging uses pulsed radar waveforms that have high peak transmission power to combat heavy path loss. Communication satellites have much lower transmission power since only one-direction propagation loss, either from satellite to ground or from ground to satellite, is encountered. They do not need to consider the extremely weak echo signals $\hat{s}_{\mathbf{r}'}(t)$.

III. SATELLITE CONSTELLATION IMAGING AND PERFORMANCE ANALYSIS

A. Delay-sensitive signal processing

If a communication signal is used, the transmitted signal can be written as

$$p(t) = \sum_{k=0}^{K-1} b_k g(t - kT_s) e^{j2\pi f_c t}, \qquad (2)$$

where b_k is the kth symbol, T_s is the symbol duration, f_c is the carrier frequency, $g(t)$ is the normalized baseband pulse such as the root raised cosine pulse waveform, and K is the total number of symbols. The received signal (1) thus becomes

$$\hat{s}_{\mathbf{r}'}(t) = \int_{\mathbf{r}} \sigma_{\mathbf{r}} \sum_{k=0}^{K-1} b_k g(t - kT_s - \tau_k) e^{j2\pi(f_c + f_d)(t - \tau_k)} d\mathbf{r}$$
$$+ \hat{v}_{\mathbf{r}'}(t), \qquad (3)$$

where τ_k is the propagation delay and f_d is the Doppler-shifting.

The difference between imaging signal processing and communication signal processing is that the former does not need to detect each symbol b_k. But rather, it just needs to use a correlator to compress $\hat{s}_{\mathbf{r}'}(t)$ into a single data sample. Considering this, a special advantage of using communication signals is that K can be arbitrarily large to enhance correlation gain. We propose to use large K to provide sufficient gain to mitigate the heavy propagation loss. However, this introduces a special delay issue that we must address, i.e. τ_k is no longer the constant $\tau_{\mathbf{r}'\mathbf{r}}$. But rather, it varies among symbols and the variance becomes significant when K is large.

Proposition 1. Let the satellite speed be the vector $\mathbf{u} = [u_x, u_y, u_z]^T$, the satellite position at $k = 0$ be $\mathbf{r}' = [x', y', z']^T$, and the target location be $\mathbf{r} = [x, y, z]^T$. Then

$$\tau_k = \frac{2(\mathbf{r}' + kT_s\mathbf{u} - \mathbf{r})^T\mathbf{u} - 2c\|\mathbf{r}' + kT_s\mathbf{u} - \mathbf{r}\|}{c^2 - \|\mathbf{u}\|^2}, \quad (4)$$

where $(\cdot)^T$ denotes transpose and $\|\cdot\|$ is norm.

Proof: During the symbol interval k, the symbol b_k is transmitted at time kT_s, reflected by the target, and received by the satellite after τ_k seconds. The signal's traveling distance is $c\tau_k = \|\mathbf{r}' + kT_s\mathbf{u} - \mathbf{r}\| + \|\mathbf{r}' + (kT_s + \tau_k)\mathbf{u} - \mathbf{r}\|$, where the first term in the right-hand-side is the distance from the satellite to the target while the second term is the distance from the target to the new satellite location after τ_k seconds. Move $\|\mathbf{r}' + kT_s\mathbf{u} - \mathbf{r}\|$ to the left-hand-side, and take the square of both sides, i.e. $(c\tau_k - \|\mathbf{r}' + kT_s\mathbf{u} - \mathbf{r}\|)^2$. After some tedious but straightforward deductions, we can get (4). $\square$

Note that (4) is for the same satellite transmission and receiving only, but can be easily extended to multiple different receiving satellite cases. From (4) we can readily see that the difference between the delay τ_0 and τ_{K-1} can be much larger than the symbol during T_s with large K. The receiver needs to calculate the delay τ_k using (4) and use the modified waveform

$$\hat{p}(t) = \sum_{k=0}^{K-1} b_k g(t - kT_s - \tau_k)e^{j2\pi(f_c + f_d)(t - \tau_k)} \quad (5)$$

as a correlator to demodulate (or, pulse-compress) the received signal into a scalar data sample

$$s_{\mathbf{r}'} = \int \hat{s}_{\mathbf{r}'}(t)\hat{p}^*(t)dt = \int_{\mathbf{r}}\sigma_{\mathbf{r}}\int_t |\hat{p}(t)|^2 dt d\mathbf{r} + v_{\mathbf{r}'}, \quad (6)$$

where $(\cdot)^*$ is complex conjugation and $v_{\mathbf{r}'}$ denotes noise.

In practice, however, it is inconvenient to generate a dynamic correlator $\hat{p}(t)$ for each satellite location $\mathbf{r}'$ in real-time. A fixed correlator is preferred. For this, we can exploit the property that the delay τ_k is approximately a linear function of k with $\|\mathbf{r}' - \mathbf{r}\|$ as the y-intercept coefficient. This means we can estimate $\hat{\tau}_k$ with a fixed reference $\mathbf{r}' - \mathbf{r}$ and use it to design the correlator. The difference between $\hat{\tau}_k$ and τ_k is approximately a constant which we write as $\tau_{\mathbf{r}'\mathbf{r}} = \hat{\tau}_k - \tau_k$. The data sample obtained at the antenna position $\mathbf{r}'$ is thus

$$s_{\mathbf{r}'} = \int_t |\hat{p}(t)|^2 dt \int_{\mathbf{r}}\sigma_{\mathbf{r}}e^{j2\pi(f_c + f_d)\tau_{\mathbf{r}'\mathbf{r}}}d\mathbf{r} + v_{\mathbf{r}'}. \quad (7)$$

Note that we have assumed the Doppler-shift f_d is constant and the flight trajectory is a straight line during the transmission of the K symbols. This is reasonable because their variations are much less than the delay variations. However, if K is too large to maintain the assumptions, we can compensate for them by considering f_d and $\mathbf{r}'_k$ in τ_k expression (4).

If $p(t)$ is the FMCW radar signal, the data sample can be obtained similarly. In this case, $p(t) = e^{j2\pi(f_c t + 0.5\beta t^2)}$ with sweeping frequency β. Due to the extremely long propagation delay, we need to design the $p(t)$ with a much-reduced duration [10]. For example, we can design the waveform based on a much-reduced reference propagation distance and transmit the FMCW waveform with relatively long interruptions. This might degrade the potential pulse compression and pulse combining gains. After de-chirping [12], we can get a data sample at the antenna location $\mathbf{r}'$ in the same form as (7). Delays can be mitigated similarly as (6) by converting (4) from τ_k to $\tau(t)$ and kT_s to t.

B. Image reconstruction with irregular satellite locations

For 2D imaging, the goal is to reconstruct a target image $\mathbf{X}$ with $I \times J$ pixels, whose elements (or pixel values) are

$$X_{ij} = \sigma_{\mathbf{r}}\Delta x \Delta y, \quad 0 \leq i \leq I - 1, 0 \leq j \leq J - 1. \quad (8)$$

The target location $\mathbf{r} = (x, y, z_0)$ is discretized into

$$x = i\Delta x + x_0, \quad y = j\Delta y + y_0, \quad (9)$$

where Δx and Δy are discretizing step sizes, x_0 and y_0 are shifts. The pixel strength $|X_{ij}|$ depends on the target reflection coefficient $\sigma_{\mathbf{r}}$ and the target area $\Delta x \Delta y$ covered by this pixel. The values of Δx and Δy can be chosen according to the theoretical imaging resolution ΔX and ΔY. In this paper, we use $\Delta x = \Delta X$ and $\Delta y = \Delta Y$.

The image pixels X_{ij} are estimated from the received data samples $s_{\mathbf{r}'}$. To construct an image of $N = IJ$ pixels, we usually require that the number of data samples be much larger than N. Although we usually have just a finite, and usually small, number of valid satellites passing over a target, each valid satellite can conduct a lot of sensing operations and acquire a lot of data samples. As an example, Fig. 1 (a) shows the STARLINK-71 satellite moves along its orbit and passes over the target located in Binghamton, NY. It can keep sensing the target until flying out of the sensing area. The sensing area is determined by the elevation or viewing angle θ of the target (see Fig. 2). Each satellite can collect a huge amount of sensing data. Therefore, the total number of data samples can be much larger than N.

However, the challenge is that the sensor locations can not form a 2D regular grid with a half-wavelength grid distance. Instead, the data samples are obtained from a set of arbitrary satellite locations on a set of satellite trajectories. This means many conventional SAR imaging algorithms such as the Range Migration Algorithm (RMA) and the Matched Filter Algorithm (MFA) [14] can not be applied because they assume a regular sensor grid to apply 2D FFT. Fortunately, we have studied this problem and developed appropriate algorithms to

reconstruct images with irregular sensor locations in [15]. The difference between this paper and [15] is that data samples are obtained from a few trajectories, not random locations within a 2D grid. We adopt the simpler algorithm which we called the Back Propagation Algorithm (BPA) in [15] because it allows us to analyze pixel signal-to-noise ratio (SNR) conveniently. We will show by simulations that BPA is reliable with data samples obtained from a few satellite trajectories, which was not studied in [15].

To construct the image, we stack the columns of $\mathbf{X}$ into an N-dimensional column vector $\mathbf{x} = \text{vec}(\mathbf{X})$. Assume we have collected M data samples from M satellite sensing positions $\mathbf{r}'_m = (x'_m, y'_m, z'_m)$, $m = 0, \cdots, M - 1$. We stack the data into an M-dimensional column vector $\mathbf{y}$, whose mth element is $y_m = s_{\mathbf{r}'_m}$. Then we have

$$\mathbf{y} = \mathbf{H}\mathbf{x} + \mathbf{v}, \tag{10}$$

where the vector $\mathbf{v}$ includes noise, interference, and clutter. The element of the $M \times N$ matrix $\mathbf{H}$ is

$$H_{mn} = e^{j4\pi R_{mn}/\lambda} \tag{11}$$

where λ is the wavelength and

$$R_{mn} = R_{m,jI+i} = ((x'_m - i\Delta x - x_0)^2 \\ + (y'_m - j\Delta y - y_0)^2 + (z'_m - z_0)^2)^{1/2} \tag{12}$$

is the distance between the antenna and the image pixel. Note that this is obtained based on (7) where the movement-induced Doppler and satellite location difference have been compensated.

Based on (10), BPA reconstructs the image as

$$\hat{\mathbf{x}} = \mathbf{H}^H \mathbf{y}. \tag{13}$$

where $(\cdot)^H$ is the Hermitian transpose. The computational complexity is $O(MN)$. The new imaging method is outlined in Algorithm 1.

Algorithm 1 Satellite Constellation Imaging Algorithm

1: **Sensing**: At each satellite position $\mathbf{r}'$, transmit signal $p(t)$ (2), receive signal $\hat{s}_{\mathbf{r}'}(t)$ (3), conduct correlation (6) to get data sample $s_{\mathbf{r}'}$ (7).
2: **Imaging**: Stack $s_{\mathbf{r}'}$ to data vector $\mathbf{y}$, construct matrix $\mathbf{H}$ (11), and calculate image $\hat{\mathbf{x}}$ via (13).

C. High-resolution imaging performance analysis

Proposition 2. The imaging resolution is

$$\Delta X = \Delta Y = \frac{\lambda}{4}\tan\theta. \tag{14}$$

Proof. Following the SAR imaging principle [15], the imaging resolution is

$$\Delta X = \Delta Y = \frac{\lambda R}{2D} \tag{15}$$

where R is the distance between the satellites and the target, and D is the array aperture in each dimension [12]. D is

determined by the satellite height and the target elevation angle θ. From Fig. 2 we have $\tan\theta = R/(D/2)$, which leads to the resolution expression (14). $\qquad\square$

It can be seen that signals with centimeter wavelengths λ can guarantee sub-centimeter imaging resolutions as long as there are a sufficient number of valid satellites in the desired elevation angle θ.

One of the major concerns for high-resolution satellite imaging is the SNRs of the received signal (3) and the calculated pixel (13). The first SNR is constrained by the limited transmission power of communication signals and large propagation loss. The second SNR is constrained by the limited reflection strength from the tiny pixel area $\Delta x \Delta y$. The communication satellites are designed for one-way transmission between the satellite and the ground device only while for sensing and imaging we have to consider the strength of the echo signal received by the satellite antenna instead. These issues have not been addressed well in the literature.

From radar principles [12], the received signal strength is

$$P_r = \frac{P_t G_t G_r \lambda^2 \sigma}{(4\pi)^3 R_1^2 R_2^2 L_s}, \tag{16}$$

where P_r is the received signal power, P_t is the transmission power, G_t is the transmitter antenna gain, G_r is the receiver antenna gain, σ is the radar cross section (RCS) (sum of $|\sigma_{\mathbf{r}}|^2$), R_1 is the distance from the transmitting antenna to the target, R_2 is the distance from the target to the receiving antenna, and L_s is the system loss factor.

The SNR of the received signal (3) is

$$\text{SNR}_s = \frac{P_t G_t G_r \lambda^2 \sigma}{(4\pi)^3 R_1^2 R_2^2 k_0 T B F L_s}, \tag{17}$$

where k_0 is Boltzmann's constant, T is the nominal scene noise temperature, F is the receiver noise factor, and B is the signal bandwidth. The SNR_s is usually small due to the weak echo signal. The satellite receiver relies on a high enough correlation gain K to conduct the successful demodulation.

Furthermore, we can exploit both the correlation gain and sensor data combining gain to enhance pixel SNR.

Proposition 3 Under some mild statistical assumptions, when constructing a 2D image with discretization step sizes Δx and Δy using M data samples, the pixel SNR is

$$\text{SNR}_p = KM\Delta x \Delta y \text{SNR}_s \tag{18}$$

Proof: For communication signals with normalized pulse waveform, the correlation gain is $\int_t |\hat{p}(t)|^2 dt = K$, which can be easily seen from (5). In (7), the power of the signal part is increased by K^2 while that of the noise part is increased by K. Comparing (7) and (17), it can be readily seen that the SNR of the data sample $s_{\mathbf{r}'}$ is $K\text{SNR}_s$, which is also the SNR of the elements of $\mathbf{y}$ in (10). The gain of the sensor data combiner can be estimated based on (13). Consider the pixel $\hat{x}_i$ (i.e., the ith element of $\hat{\mathbf{x}}$). It is the linear combination of all the satellite data samples through

$$\hat{x}_i = \mathbf{h}_i^H \mathbf{y} = \mathbf{h}_i^H \mathbf{H}\mathbf{x} + \mathbf{h}_i^H \mathbf{v} \tag{19}$$

where $\mathbf{h}_i$ is the ith column of $\mathbf{H}$ and has dimension $M \times 1$. From (11), we can see that all the elements of $\mathbf{h}_i$ and $\mathbf{H}$ are complex exponential in the form of $e^{j2\pi d/\lambda}$ where d is the propagation distance. It is reasonable to assume that the phases $2\pi d/\lambda$ are independent, identically distributed random variables with uniform distribution in $[0, 2\pi]$. When $M \gg N$, we have $\mathbf{h}_i^H \mathbf{H}_i = [0, \cdots, 0, M, 0, \cdots, 0]$ almost surely, where M is the ith element and is the only non-zero element. Comparing $\hat{x}_i$ over $s_{\mathbf{r}'}$, the signal part has a power gain $M^2 \Delta x \Delta y$, while the noise part has a power gain of M, which leads to the pixel SNR (18). $\qquad\square$

From (18), we can see that we can use a longer sensing signal (larger K) and collect more data samples (larger M) to boost pixel SNR. SAR imaging community often uses the Noise Equivalent Sigma Zero (NESZ) to describe imaging quality, which in our case is just $\text{NESZ} = \sigma/\text{SNR}_p$.

IV. SIMULATION AND EXPERIMENT

In this section, first, we use simulations to verify the new imaging algorithm and compare it with conventional SAR imaging. Then, since satellite data are not available, we use practically measured millimeter wave radar data to demonstrate the new imaging algorithm.

A. Satellite Imaging Simulation

For simulations, we used the SpaceX Starlink satellite constellation data obtained from Starlink's two-line element (TLE) file https://celestrak.org to get the orbital information of all the satellites. The TLE file of Oct. 21, 2022, consisted of 3195 Starlink satellites. We simulated a target located at the coordinates of Binghamton, NY. With an elevation angle $\theta = 30°$, we had 555 valid satellites. Their distance to the target was around $R = 462$ km. This means we had an effective radar aperture of 1600×1600 km^2, i.e. $D = 1600$ km. The theoretical resolution is thus $\Delta X = \Delta Y = 0.0037$ meters according to (14) or (15).

We applied the typical Starlink signal parameters [9]: Carrier frequency $f_c = 11.7$ GHz ($\lambda = 2.6$ centimeter), bandwidth $B = 250$ MHz, antenna gain $G_t = G_r = 40$ dB, receiver noise factor $F = 5$ dB, system loss $L_s = 5$ dB, transmit power $P_t = 67$ dBm. Since we considered the average SNR, we let $R_1 = R_2 = R$. Assuming $\sigma = 100$ square meters, we had $P_r = -133$ dBm according to (16), higher than the typical satellite receiver's sensitivity of -135 dBm, which means the receiver could detect the echo correctly.

From (17), we had $\text{SNR}_s = -18$ dB, which was too small. With $K = 10^4$, we had a correlation gain of 40 dB to boost SNR_s to 22 dB, which then had sufficient margin to tolerate even any extra severe weather-related path loss. Furthermore, assuming $M = 10^5$, from (18) we had $\text{SNR}_p = 23$ dB under pixel discretization stepsizes $\Delta x = \Delta y = .0037$ meters, which is high enough for imaging.

We used MATLAB radar, phased array, and satellite toolboxes to simulate signal propagation. We created a target consisting of 4 points on the inner circle of radius 0.02 meters and 8 points on the outer circle of radius 0.05 meters, as shown
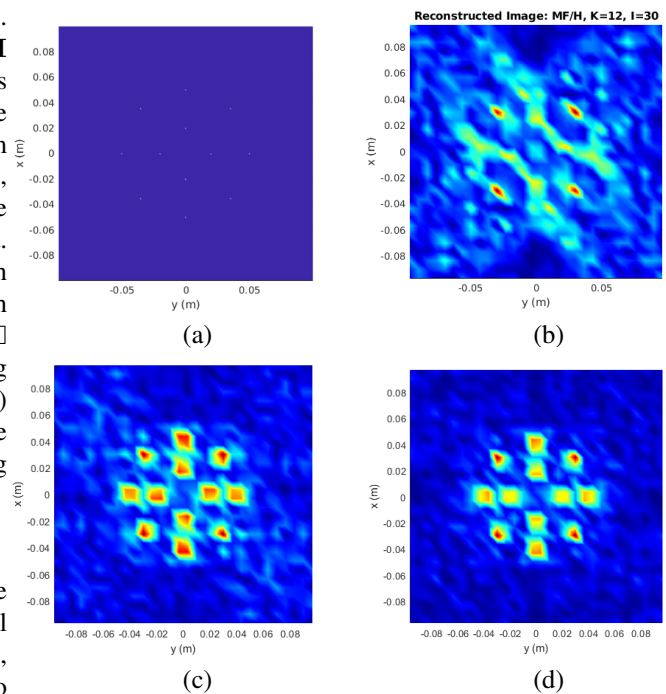

Fig. 3. (a): True target with 12 white dots. (b)-(d): Images reconstructed by the proposed algorithm using 12, 96, and 384 satellites, respectively.

in Fig. IV-A(a). We simulated FMCW, DVB-S2X, and 5G waveforms as satellite signals. For 5G, we used only the cell searching signal with $K = 2 \times 10^4$ symbols.

Fig. IV-A(b)-(d) shows the reconstructed images using the 5G waveform. The imaging qualities were also compared in Table I in terms of peak-signal-to-noise ratio (PSNR), structural similarity method (SSIM) [16], and mean square error (MSE) between the reconstructed image and the true image. The conventional SAR did not give any meaningful image because its resolution was too low. In contrast, the proposed algorithm could give clear target images in all the configurations listed in the table, even with as less as 12 satellites.

Next, we used simulations to evaluate the robustness of the method to inaccurate satellite position and phase incoherence among satellites. We found that random errors equivalent to a 1-centimeter standard deviation of satellite position errors reduced imaging PSNR by about 2.5 dB. Error deviation of 1 millimeter led to negligible degradation, but a 0.1-meter deviation made images unrecognizable. Note that satellite position accuracy is practically at the centimeter level (see https://igs.org) and phase incoherence compensation is a routine technique in existing SAR.

Therefore, the proposed method can successfully provide high-resolution images at sub-centimeter resolution even when only a small set of satellites are used and when there are various positioning and phase inaccuracies.

B. Real Measured Data Experiment

In this experiment, we resorted to the real measured millimeter-wave imaging data published in [14] to demonstrate

Algorithm	Res. (m)	PSNR(dB)	SSIM	MSE
SAR (1)	0.85	8.6805	0.0081	0.1355
5G(384)	0.0037	15.1216	0.0494	0.0307
5G(192)	0.0037	14.9713	0.0478	0.0318
5G(96)	0.0037	13.4933	0.0371	0.0447
5G(48)	0.0037	12.6132	0.0354	0.0548
5G(24)	0.0037	12.8188	0.0366	0.0523
5G(12)	0.0037	11.3776	0.0147	0.0728
DVB(384)	0.0037	14.9370	0.0397	0.0323
DVB(192)	0.0037	14.8166	0.0350	0.0330
DVB(96)	0.0037	14.1155	0.0285	0.0388
DVB(48)	0.0037	13.9949	0.0308	0.0399
DVB(24)	0.0037	12.8442	0.0221	0.0519
DVB(12)	0.0037	11.2367	0.0071	0.0752
FMCW(384)	0.0037	15.2110	0.0419	0.0312
FMCW(192)	0.0037	15.0548	0.0378	0.0301
FMCW(96)	0.0037	14.6919	0.0355	0.0341
FMCW(48)	0.0037	13.4799	0.0225	0.0449
FMCW(24)	0.0037	12.9010	0.0207	0.0513
FMCW(12)	0.0037	12.2147	0.0182	0.0601

Lines(Data Percent)	PSNR (dB)	SSIM	MSE
All (100%)	27.1	0.83	-
150 (51%)	26.0612	0.6885	0.0025
100 (34%)	20.7141	0.4907	0.0085
75 (28%)	21.0266	0.4674	0.0079
50 (21%)	18.9880	0.3608	0.0126
30 (11%)	13.8393	0.1735	0.0413
20 (6%)	13.6054	0.1948	0.0436

the effectiveness of our imaging algorithm. Specifically, to emulate the straight trajectories of a few satellites, we used the data along some straight lines only. Because the total data amount was very small in this data set, we had to use a lot of straight lines. Results in Fig. 4 show that using a portion of the data on straight-line trajectories could reconstruct the image successfully. The imaging reconstruction quality was quantitatively compared in Table. II. We can see that the imaging quality reduced gracefully with the number of straight lines or the percentage of data used.
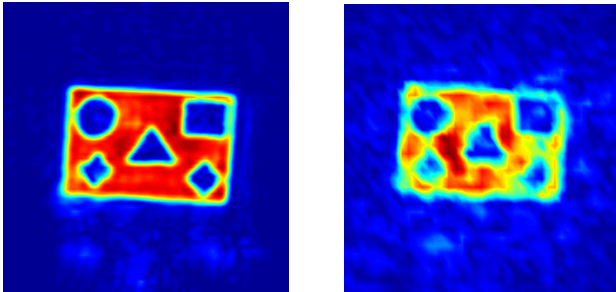

Fig. 4. Millimeter wave radar data reconstructed images. Left: use all the data. Right: use 28% data located on 75 straight lines.

V. CONCLUSIONS

There has been a great interest in deploying large-scale LEO satellite constellations for global communications, but there is not sufficient attention given to their capability of sensing and imaging. This paper demonstrates that using a few LEO satellites can generate ground images with super high resolution of sub centimeters, a mission almost impossible with existing satellite SAR imaging. This paper uncovers the great potential of integrated communication and sensing research in LEO satellite constellations.

REFERENCES

[1] M. Giordani and M. Zorzi, "Non-terrestrial networks in the 6g era: Challenges and opportunities," *IEEE Network*, vol. 35, no. 2, pp. 244–251, 2020.

[2] N. Pachler, I. del Portillo, E. F. Crawley, and B. G. Cameron, "An updated comparison of four low earth orbit satellite constellation systems to provide global broadband," in *2021 IEEE international conference on communications workshops (ICC workshops)*, pp. 1–7, IEEE, 2021.

[3] I. Del Portillo, B. G. Cameron, and E. F. Crawley, "A technical comparison of three low earth orbit satellite constellation systems to provide global broadband," *Acta astronautica*, vol. 159, pp. 123–135, 2019.

[4] F. Liu, Y. Cui, C. Masouros, J. Xu, T. X. Han, Y. C. Eldar, and S. Buzzi, "Integrated sensing and communications: Towards dual-functional wireless networks for 6g and beyond," *IEEE journal on selected areas in communications*, 2022.

[5] U. K. Majumder, E. P. Blasch, and D. A. Garren, *Deep Learning for Radar and Communications Automatic Target Recognition*. Artech House, 2020.

[6] N. E. Alexander, B. Alderman, F. Allona, P. Frijlink, R. Gonzalo, M. Hägelen, A. Ibáñez, V. Krozer, M. L. Langford, E. Limiti, *et al.*, "Terascreen: Multi-frequency multi-mode terahertz screening for border checks," in *Passive and Active Millimeter-Wave Imaging XVII*, vol. 9078, p. 907802, International Society for Optics and Photonics, 2014.

[7] K. B. Cooper, R. J. Dengler, N. Llombart, B. Thomas, G. Chattopadhyay, and P. H. Siegel, "Thz imaging radar for standoff personnel screening," *IEEE Transactions on Terahertz Science and Technology*, vol. 1, no. 1, pp. 169–182, 2011.

[8] S. S. Ahmed, A. Schiessl, and L.-P. Schmidt, "A novel fully electronic active real-time imager based on a planar multistatic sparse array," *IEEE Transactions on Microwave Theory and Techniques*, vol. 59, no. 12, pp. 3567–3576, 2011.

[9] A. Sayin, M. Cherniakov, and M. Antoniou, "Passive radar using starlink transmissions: A theoretical study," in *2019 20th International Radar Symposium (IRS)*, pp. 1–7, IEEE, 2019.

[10] P. Hoogeboom, R. Hanssen, M. Pastena, E. Imbembo, P. van Duijn, M. Otten, S. Monni, P. Hoogeboom, R. Hanssen, M. Pastena, *et al.*, "Panelsar, an fmcw based x-band smallsat sar for infrastructure monitoring," in *The 27th Annual AIAA/USU Conference on Small Satellites, Logan, USA*, pp. 1–5, 2013.

[11] Y. Liu, Y. K. Deng, R. Wang, and O. Loffeld, "Bistatic fmcw sar signal model and imaging approach," *IEEE Transactions on Aerospace and Electronic Systems*, vol. 49, no. 3, pp. 2017–2028, 2013.

[12] M. A. Richards, J. Scheer, W. A. Holm, and W. L. Melvin, *Principles of modern radar*. Citeseer, 2010.

[13] I. Pisciottano, F. Santi, D. Pastina, and D. Cristallini, "Dvb-s based passive polarimetric isar—methods and experimental validation," *IEEE Sensors Journal*, vol. 21, no. 5, pp. 6056–6070, 2020.

[14] M. E. Yanik and M. Torlak, "Near-field mimo-sar millimeter-wave imaging with sparsely sampled aperture data," *IEEE Access*, vol. 7, pp. 31801–31819, 2019.

[15] X. Li and Y. Chen, "Lightweight 2d imaging for integrated imaging and communication applications," *IEEE Signal Processing Letters*, vol. 28, pp. 528–532, 2021.

[16] A. Hore and D. Ziou, "Image quality metrics: Psnr vs. ssim," in *2010 20th international conference on pattern recognition*, pp. 2366–2369, IEEE, 2010.